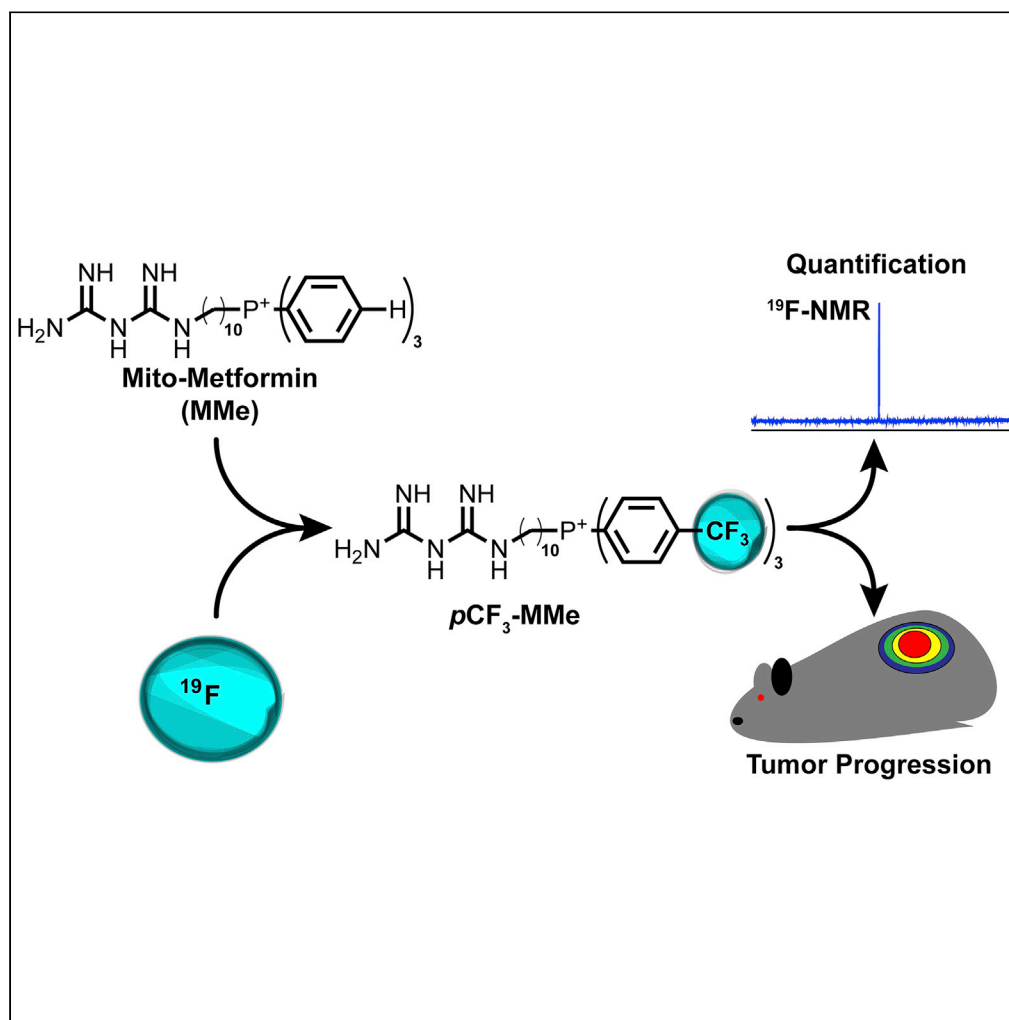Article

Fluorinated triphenylphosphonium analogs improve cell selectivity and *in vivo* detection of mito-metformin

Mahmoud AbuEid, Robert F. Keyes, Donna McAllister, ..., Pradeep Chaluvally-Raghavan, Brian C. Smith, Michael B. Dwinell

brismith@mcw.edu (B.C.S.)
mdwinell@mcw.edu (M.B.D.)

Highlights

Adding fluorine to triphenylphosphonium cation increases cancer cell selectivity

Fluorination retains the anti-proliferative activity of mitochondria-targeted metformin

Fluorinated mitochondria-targeted metformin has a half-life of nearly 2 h

Fluorinated mitochondria-targeted metformin has reduced toxicity *in vivo*

Article

Fluorinated triphenylphosphonium analogs improve cell selectivity and *in vivo* detection of mito-metformin

Mahmoud AbuEid,[1,2] Robert F. Keyes,[3,4] Donna McAllister,[1] Francis Peterson,[3,4] Ishaque Pulikkal Kadamberi,[5] Daniel J. Sprague,[4,6] Pradeep Chaluvally-Raghavan,[5] Brian C. Smith,[3,4,*] and Michael B. Dwinell[1,2,7,*]

SUMMARY

Triphenylphosphonium (TPP⁺) conjugated compounds selectively target cancer cells by exploiting their hyperpolarized mitochondrial membrane potential. To date, studies have focused on modifying either the linker or the cargo of TPP⁺-conjugated compounds. Here, we investigated the biological effects of direct modification to TPP⁺ to improve the efficacy and detection of mito-metformin (MMe), a TPP⁺-conjugated probe we have shown to have promising preclinical efficacy against solid cancer cells. We designed, synthesized, and tested trifluoromethyl and methoxy MMe analogs (*p*CF₃-MMe, *m*CF₃-MMe, and *p*MeO-MMe) against multiple distinct human cancer cells. *p*CF₃-MMe showed enhanced selectivity toward cancer cells compared to MMe, while retaining the same signaling mechanism. Importantly, *p*CF₃-MMe allowed quantitative monitoring of cellular accumulation via ¹⁹F-NMR *in vitro* and *in vivo*. Furthermore, adding trifluoromethyl groups to TPP⁺ reduced toxicity *in vivo* while retaining anti-tumor efficacy, opening an avenue to de-risk these next-generation TPP⁺-conjugated compounds.

INTRODUCTION

Increases in the mitochondrial membrane potential are a recognized characteristic in multiple types of solid and liquid cancers.[1–4] It remains unclear if changes in membrane potential are causal events or secondary events in cancer progression. The molecular mechanisms underlying mitochondrial membrane hyperpolarization remain enigmatic but have been experimentally exploited to selectively target cancer cells instead of normal cells. For example, rhodamine-123, mitochondria-penetrating peptides, Szeto-Schiller peptides, and triphenylphosphonium cation (TPP⁺)-conjugated compounds have all been synthesized to selectively target cancer cells.[5–7] To date, TPP⁺-conjugated compounds have demonstrated the most promising *in vitro* and *in vivo* data.[8–13] TPP⁺-conjugated compounds consist of the mitochondria-targeting TPP⁺ moiety, a linker typically consisting of an aliphatic carbon chain, and a functional cargo.[12–15] TPP⁺-conjugated compounds were used to uncover the mechanism of coupling oxidative phosphorylation to mitochondrial membrane potential and, subsequently, to understand the role of oxidative metabolism in cancer.[16] Moreover, early efforts by Murphy et al. focused on using the antioxidant Mito-Q, a TPP⁺-conjugated synthetic analog of coenzyme Q10, ubiquinone, to understand the role of mitochondrial redox recycling in disease progression.[17,18] For over a decade, TPP⁺-conjugated compounds have been examined as tumor-selective anti-cancer agents, including mitochondria-targeted-3-carboxy-proxyl nitroxide, mitochondria-targeted-magnolol, mitochondria-targeted-metformin (MMe) and others. Each demonstrated broad anti-tumor efficacy by inhibiting complex I of the electron transport chain and activating energy-sensing signaling pathways.[8,9,11,19,20] These TPP⁺-conjugated mitochondria-targeted compounds are examples of the functional consequences of changing the cargo. Changes in the carbon chain linker may skew TPP⁺-conjugated compounds to target complex III over complex I.[19] While previous efforts have focused on modifying the aliphatic linker or the cargo, very few studies have investigated the functional and biological consequences of modifying the TPP⁺ moiety.[21]

The conventional wisdom underlying the use of TPP⁺ was that the large ionic radius, diffuse positive charge, and lipophilic nature allowed conjugated compounds to cross lipid bilayers and accumulate in the more negative inside of mitochondria.[13–15] Most structural modifications to TPP⁺-conjugated agents have

[1]Department of Microbiology & Immunology, Medical College of Wisconsin, 8701 Watertown Plank Road, Milwaukee, WI 53122, USA

[2]Center for Immunology, Medical College of Wisconsin, 8701 Watertown Plank Road, Milwaukee, WI 53122, USA

[3]Department of Biochemistry, Medical College of Wisconsin, 8701 Watertown Plank Road, Milwaukee, WI 53122, USA

[4]Program in Chemical Biology, Medical College of Wisconsin, 8701 Watertown Plank Road, Milwaukee, WI 53122, USA

[5]Department of Obstetrics & Gynecology Medical College of Wisconsin, Milwaukee, WI 53122, USA

[6]Department of Cell Biology, Neurobiology, and Anatomy, Medical College of Wisconsin, Milwaukee, WI 53122, USA

[7]Lead contact

*Correspondence:
brismith@mcw.edu (B.C.S.),
mdwinell@mcw.edu (M.B.D.)
https://doi.org/10.1016/j.isci.2022.105670

focused on modifying the length of the linker connecting TPP[+] to cargo to fine-tune lipophilicity and localization of the mitochondria-targeted compound. A recent report has shown that TPP[+] modifications can be employed to dissociate mitochondrial localization from functional effects on mitochondrial respiration.[21] Notably, this report demonstrated a strong role for fluorine modifications in enhancing mitochondrial localization. Fluorine has different physical and chemical properties from other elements, including bond length, van der Waals radius, van der Waals volume, and electronegativity.[22] Fluorine's small van der Waals radius, 1.46 Å, can easily sterically replace hydrogen with a van der Waals radius of 1.2 Å.[23] Unlike other halogens, non-polarizable fluorine does not participate in halogen bonding. Finally, the introduction of fluorine allows fine-tuning of the electrostatic properties of the compound based on the number and regiochemical placement of the fluorine atoms.[24] The ^{19}F isotope has 100% natural abundance and a +1/2-spin, resulting in an easily detectable NMR-active nucleus. As fluorinated compounds are scarce in nature, the introduction of ^{19}F to a compound enables the use of ^{19}F NMR detection of fluorinated TPP[+]-conjugated compounds with minimal noise resulting from endogenous molecules. Thus, fluorine substitution may have the added benefit of increasing the detectability of mitochondria-targeted compounds using ^{19}F NMR or ^{18}F positron emission tomography.

Here, we rationally redesigned and tested analogs of MMe, selected for its promising preclinical results, by adding electron-withdrawing trifluoromethyl groups in the *para* and *meta* positions of the TPP[+] aryl rings (pCF$_3$-MMe and mCF$_3$-MMe). These analogs have reduced electron density on the phosphorus atom of the TPP group, which in turn improved the cell-type selectivity for cancer over normal cells. Importantly, fluorinating the TPP[+] rings had the added benefit of *in vivo* detection and quantification via ^{19}F-NMR. We also synthesized an electron-rich MMe analog containing *para*-methoxy aryl rings, pMeO-MMe, that allowed direct comparison of the effect of electron-withdrawing and electron-donating groups on the electron density of the phosphorus atom and the subsequent biological effects of TPP[+]-conjugated compounds. These data are the first to demonstrate that the addition of trifluoromethyl groups to the TPP[+] moiety enhances selectivity for cancer cells, allows reproducible measurement of the accumulation of TPP[+]-conjugated compounds within tumor and non-tumor tissues, and improves the overall safety profile of TPP[+]-conjugated compounds while maintaining potent anti-tumor efficacy *in vitro* and *in vivo*.

RESULTS

Design of next-generation mitochondria-targeted agents by direct triphenylphosphonium modification

Cationic lipophilic functional groups such as TPP[+] move across biological membranes, particularly the mitochondrial membrane, without transporters.[15] This phenomenon was previously exploited to selectively deliver metformin into cancer cells to enhance its anti-tumor efficacy and mitigate potential off-tumor side effects.[9–11] Here, we fine-tuned the partial positive charge on the phosphorus center of MMe in a stepwise fashion by adding substituents to the aryl rings of the TPP[+] moiety. Strong electron-withdrawing trifluoromethyl substituents were added to the *meta* or *para* positions of the TPP rings, mCF$_3$-MMe, and pCF$_3$-MMe, respectively (Figure S1). Trifluoromethyl substitution at the *meta* position increases the positive charge on the phosphorus center by withdrawing electrons through the aryl rings inductively. Trifluoromethyl substitution at the *para* position withdraws electrons both inductively and through resonance effects. Thus, the synthesis of each molecule enabled us to test the impact of gradients of increasing partial positive charge on the phosphorus center of the TPP[+] moiety for enhanced accumulation in the mitochondria (Figures 1C and 1D). By comparison, the partial positive charge at the phosphorus center of MMe was decreased by adding *para*-methoxy substituents to the TPP aryl rings affording pMeO-MMe (Figure S1). Methoxy substituents at the *para* position of the phenyl rings increase electron density throughout the conjugated π-system via resonance, resulting in decreased partial positive charge at the phosphorus center (Figure 1A). Ultimately, these three novel MMe analogs allowed for a controlled decrease in electron density on the phosphorus atom: pMeO-MMe > MMe $\gg$ mCF$_3$-MMe > pCF$_3$-MMe (Figure 1). With these molecules in hand, we compared the biological effects produced by varying the cationic character of the phosphorus center compared to the parent MMe compound.

Modifying triphenylphosphonium increases selectivity while maintaining anti-tumor efficacy

We previously reported broad anti-tumorigenic effects of TPP[+]-conjugated compounds, with MMe consistently 100- to 1000-fold more efficacious on pancreatic, breast, and colon cancers compared to the FDA-approved biguanide compound metformin.[8,10,11] Here, we explored the anti-tumorigenic effects of the newly synthesized trifluoromethyl and methoxy MMe analogs, pCF$_3$-MMe, mCF$_3$-MMe, and
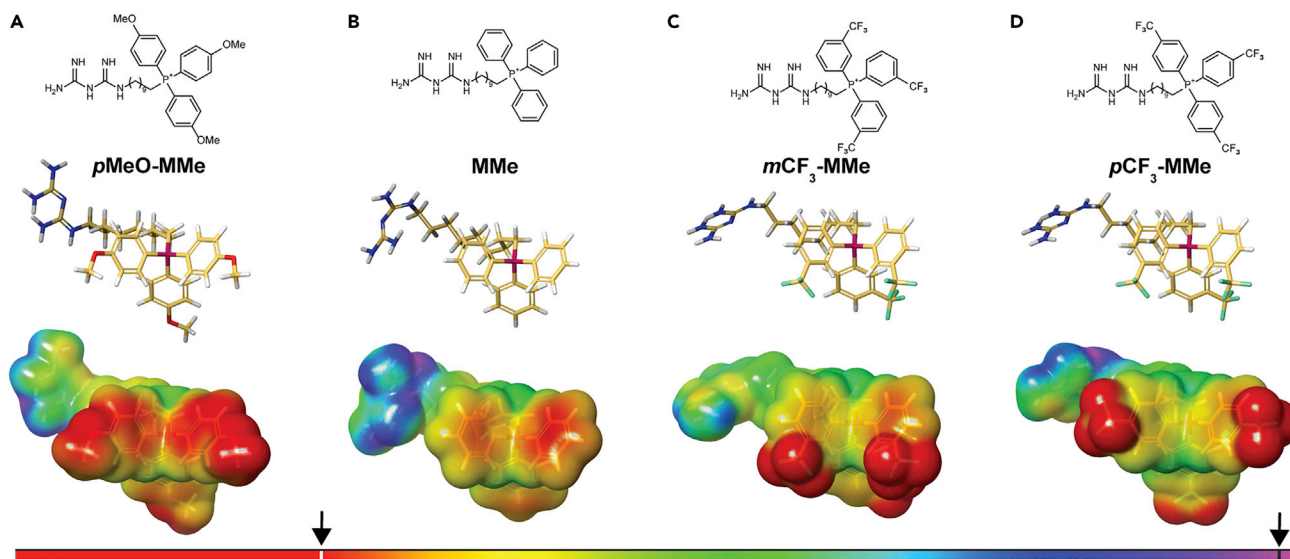
Figure 1. Impact of aryl ring substitutions on the electron density of MMe

(A–D) Chemical structures (top), stick model (middle), and electron density maps (bottom) of MMe (B) and the analogs *p*MeO-MMe (A), *m*CF$_3$-MMe (C), and *p*CF$_3$-MMe (D). The chemical stick model displays the position, bonds, and predicted three-dimensional orientation of the individual atoms within each compound. The heatmap depicts the range of electron density for all four compounds. Red indicates increased electron density (decreased partial positive charge); blue indicates decreased electron density (increased partial positive charge). The arrows and white and black markers denote the range of electron density seen for MMe.

*p*MeO-MMe, on a battery of murine (KPC1242) and human (Panc-1, AsPC-1) pancreatic, colonic (HCT-116), breast (MDA-MB-231), and ovarian (OVCAR-4, OVCAR-8) cancer cell lines. To investigate tumor cell selectivity, human pancreatic nestin-expressing cells (HPNE) were used as a surrogate for normal epithelial cells, and human pancreatic stellate cells (HPSC) were studied as a non-transformed stromal cell type. Cells were exposed to escalating concentrations of MMe, *p*CF$_3$-MMe, *m*CF$_3$-MMe, and *p*MeO-MMe (Figures 2A–2D) and percent confluency was measured as a surrogate for daily proliferation. Growth curves and photomicrographs were used to calculate IC$_{50}$ values at either 96 or 120 h (Figures 2A–2D) and confirmed that cell confluency was decreased in a concentration-dependent manner in each of the cancer cells treated with MMe (Figure S2), *p*CF$_3$-MMe (Figure S3), and *m*CF$_3$-MMe (Figure S4). Examination of *p*MeO-MMe in human pancreatic cancer cells also revealed a concentration-dependent decrease in confluence (Figure S5).

To test the off-target effects of the refined MMe analogs on normal non-transformed cells, the growth of HPNE cells (Figures S6A, S6D, and S6G), used as a surrogate for normal pancreatic ductal epithelium, or normal stromal HPSC cells (Figures S6B, S6E, and S6H) were measured in increasing concentrations of MMe, *p*CF$_3$-MMe, or *m*CF$_3$-MMe and compared to the vehicle control. Normal, non-transformed cells were more than a log-unit less sensitive to MMe, *p*CF$_3$-MMe, and *m*CF$_3$-MMe compared to cancer cells (Figures S5A–S5H). Logarithmic fitting of growth curves revealed strong growth inhibitory effects of MMe (Figures 2A–2C), *p*CF$_3$-MMe (Figures 2D–2F), and *m*CF$_3$-MMe (Figures S4A and S4B). Moreover, logarithmic fitting of growth curves demonstrated that *p*CF$_3$-MMe had the least toxic effects toward non-transformed HPNE and HPSC-1 cells compared to the parent MMe and the *m*CF$_3$-MMe analog (Figures 2A, 2C, and S4A).

Next, we determined the direct effects of MMe or *p*CF$_3$-MMe treatment on cellular proliferation by measuring Ki-67 levels; increased Ki-67 expression is associated with increased cellular growth. KPC1242 cells treated with MMe or *p*CF$_3$-MMe demonstrated a significant 20-30% reduction in Ki-67 levels after 24-h treatment (Figure 2E). Subsequent experiments focused on *p*CF$_3$-MMe as it demonstrated the highest preclinical potential with efficacy toward cancer cells and decreased toxicity toward normal cells.

*p*CF$_3$-MMe maintains bioenergetic metabolism inhibitory effects of mito-metformin

Both the parent compound metformin and mitochondria-targeted compound MMe inhibit complex I-mediated oxygen consumption and activate energy-sensing signaling pathways.[9] To determine if the newly synthesized variants retain this functional specificity, we next determined if *p*CF$_3$-MMe effectively
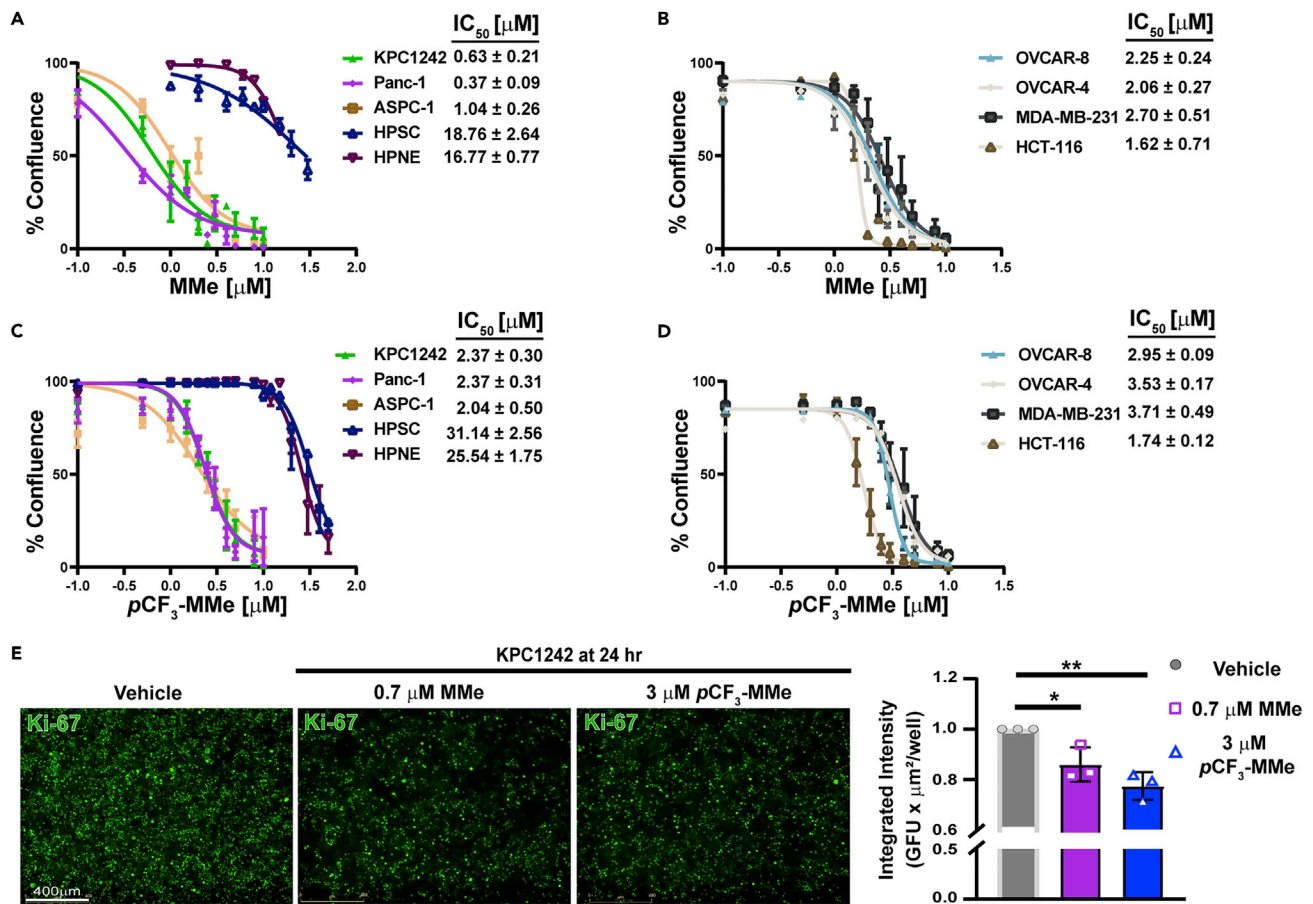
Figure 2. Growth inhibitory effects of MMe, pCF$_3$-MMe, and mCF$_3$-MMe on pancreatic, ovarian, breast, and colon cancers and non-transformed normal epithelial cells

(A–E) Logarithmic dose-response fit curves of KPC1242, Panc-1, AsPC-1, HPSC, and HPNE confluence in response to treatment with MMe (A) or pCF$_3$-MMe (C), or OVCAR-8, OVCAR-4, MDA-MB-231, and HCT-116 confluence in response to treatment with MMe (B) or pCF$_3$-MMe (D). Densitometric quantification (E) in KPC1242 cells treated with MMe (0.7 μM) or pCF$_3$-MMe (3 μM). Representative images of levels of Ki-67 (green) were recorded using the IncuCyte of KPC1242 treated with MMe (0.7 μM) or pCF$_3$-MMe (3 μM), followed by the quantification of the total integrated intensity of Ki-67. Values are mean ± SD, n = 3-4, each experiment completed in technical duplicates or triplicates. IC$_{50}$ values were calculated from confluence curves on the final day of the study as shown in Figures S2–S6. Statistical differences in panel E were determined using Student's t-test (*, $p < 0.05$; **, $p < 0.01$).

impacts mitochondrial function and/or induces bioenergetic stress. KPC1242 cells were treated for 24 h with increasing concentrations of MMe or pCF$_3$-MMe, and oxygen consumption rate (OCR) was measured as a surrogate for oxidative phosphorylation-linked mitochondrial respiration.[25,26] The Seahorse Cell Mito Stress Test, which provides a quantitative assessment of mitochondrial function that includes basal respiration, ATP-linked respiration, maximal and reserve capacities, and non-mitochondrial respiration, revealed a concentration-dependent decrease in basal OCR, ATP-linked respiration, and maximal respiratory capacity in MMe (Figure 3A) and pCF$_3$-MMe (Figure 3E) treated cells. Next, we evaluated if the observed decrease in OCR with pCF$_3$-MMe corresponded to an inhibition of mitochondrial respiratory complex I. In agreement with our previous reports,[9,11] MMe and pCF$_3$-MMe decreased complex I-derived OCR in the KPC1242 cell line in a concentration-dependent manner. This effect was attenuated by supplementing succinate, a complex II substrate, allowing bypass of complex I,[27,28] which suggests the mechanism for OCR inhibition is indeed through complex I for both MMe and pCF$_3$-MMe. Moreover, logarithmic fitting revealed potent basal OCR inhibition (Figures 3C and 3G) and complex I inhibition at IC$_{50}$ values comparable to growth inhibition (Figures 3D and 3H).

TPP-conjugated compounds effectively target the mitochondria of cancer cells.[1,9,15,17,18,29,30] Thus, we tested and compared the efficacy of pCF$_3$-MMe to target the mitochondria of cancer cells compared to
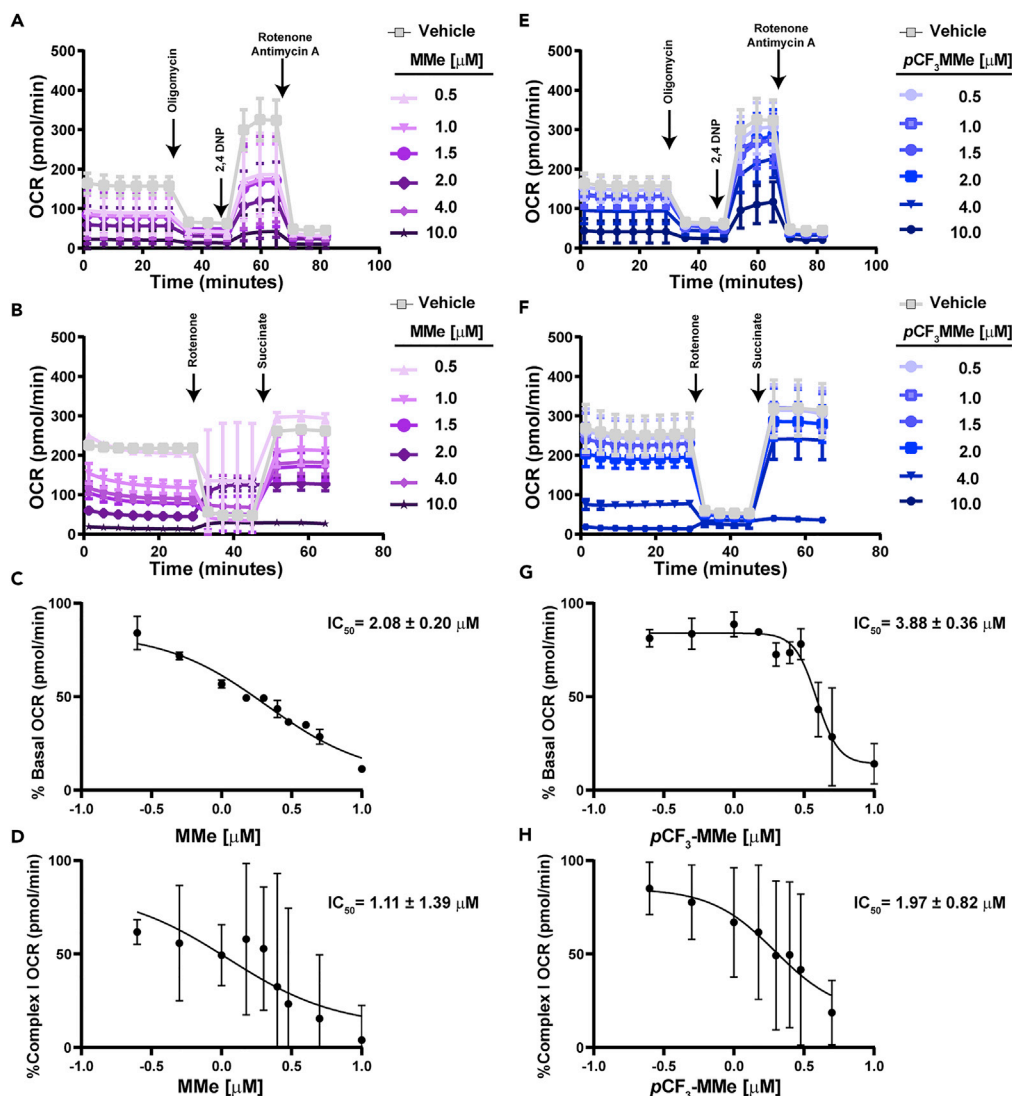
Figure 3. pCF_3-MMe inhibits complex I derived mitochondrial respiration

(A and E) Representative mitochondrial stress tests on the KPC1242 pancreatic cancer cell line preceded by 24 h treatment with MMe (A) or pCF_3-MMe (E). Injections of oligomycin (1 µg/mL), 2,4-dinitrophenol (50 µM), rotenone (1 µM), and antimycin A (10 µM) were injected as indicated by the arrows.

(B and F) Representative complex I-derived oxygen consumption rate (OCR) after 24 h treatment of increasing concentrations of MMe (B) or pCF_3-MMe (F) followed by rotenone to inhibit complex I and succinate to bypass complex I inhibition.

(C and G) Logarithmic dose-response curves of basal oxygen consumption rate in response to increasing concentrations of MMe (C) or pCF_3-MMe (G) in KPC1242 cells.

(D and H) Logarithmic dose-response curves of complex I-derived oxygen consumption rate in response to increasing concentrations of MMe (D) or pCF_3-MMe (H) in KPC1242 cells. Treated cells were normalized to vehicle (C, G, and D). Values are mean ± SD from 3 biological replicates completed in technical quadruplicate.

normal cells using tetramethylrhodamine ethyl ester perchlorate (TMRE), a cell-permeant, positively charged dye that accumulates in active mitochondria, and is released into the cytosol upon mitochondrial damage.[31,32] Differences in TMRE retention are often used to measure mitochondrial damage.[31,32] As expected,[9,21] and shown in Figures 4A–4D, MMe significantly reduced TMRE accumulation within the mitochondria of AsPC-1 measured decreased fluorescence; similarly, pCF_3-MMe significantly reduced TMRE accumulation within the mitochondria of AsPC-1 (Figures 4A and 4C). Although not significant, pCF_3-MMe demonstrated a stronger trend toward decreased TMRE accumulation compared to MMe. Consistent with
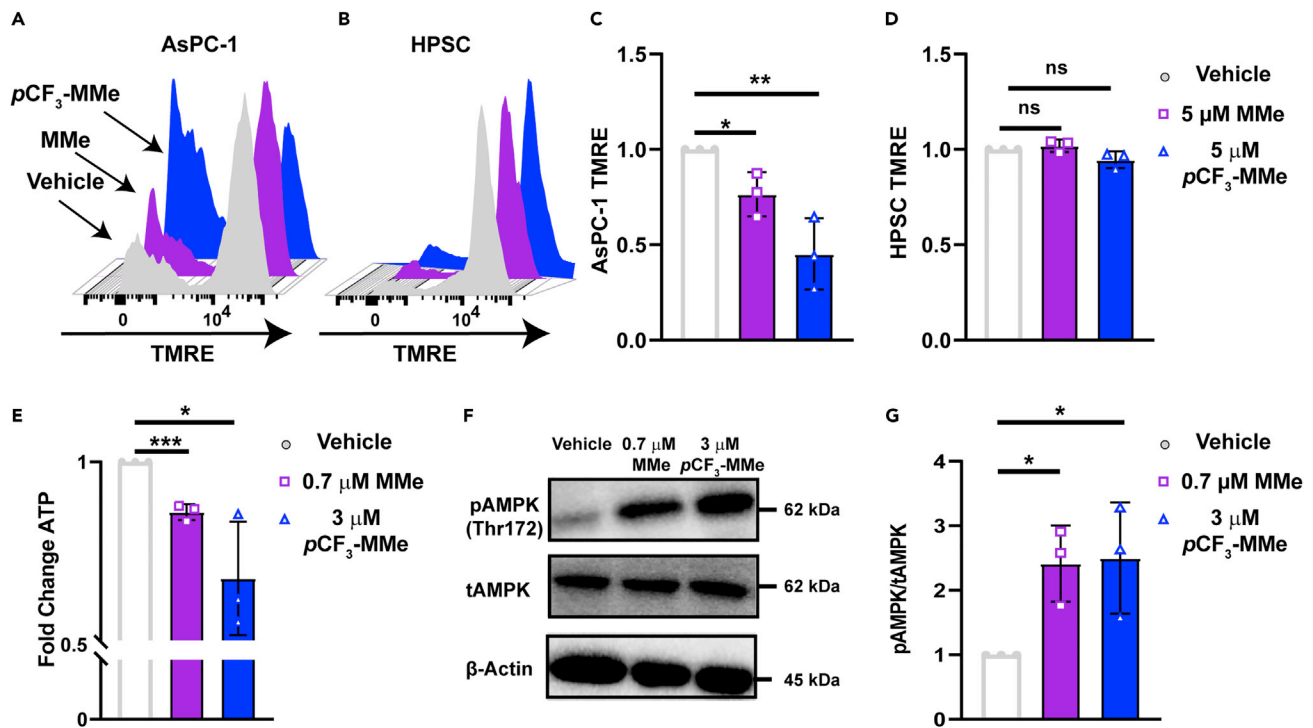
Figure 4. pCF_3-MMe selectively depolarizes mitochondria and activates bioenergetic signaling in cancer cells

(A–G) AsPC-1 and HPSC cells were serum-starved overnight, loaded with tetramethylrhodamine ethyl ester (TMRE), and treated for 1 h with the indicated concentrations of MMe or pCF_3-MMe or, as the vehicle control, DMSO. Mitochondrial TMRE retention was measured by flow cytometry. Representative histograms of n = 3 of TMRE fluorescence in AsPC-1 (A) and HPSC (B) in response to treatment. Normalized Mean fluorescence intensity of TMRE in treated AsPC-1 (C) shows the depolarization of mitochondrial membrane in response to treatment and a lack of depolarization in the HPSC cells (D). Total cellular ATP levels were analyzed using a luminescent ATP detection assay of KPC1242 cells treated with MMe (0.7 µM) or pCF_3-MMe (3 µM), and changes in ATP levels were assayed (E). Representative immunoblot analyses of phosphorylated and total AMPK levels (F) and densitometric quantification (G) in KPC1242 cells treated with MMe (0.7 µM) or pCF_3-MMe (3 µM). Representative images of levels of Ki-67 (green) were recorded using the IncuCyte of KPC1242 treated with MMe (0.7 µM) or pCF_3-MMe (3 µM), followed by the quantification of the total integrated intensity of Ki-67. Values are mean $\pm$ SD from 3 biological replicates. Statistical differences in panels A, C, and E were determined using Student's t-test (*, $p < 0.05$; **, $p < 0.01$; ***, $p < 0.001$; ns: not significant).

their selectivity toward cancer cells, both MMe and pCF_3-MMe did not affect TMRE accumulation within the HPSC cell line (Figures 4B and 4D).

The functional consequence of inhibiting mitochondria complex I and subsequently oxidative phosphorylation is a reduction of overall ATP levels in the cell.[33] We previously reported the ability of MMe to reduce ATP levels in numerous cancer cell types.[9,11] Thus, we explored if pCF_3-MMe retained similar properties. KPC1242 cells were treated with MMe or pCF_3-MMe for 24 h at concentrations that inhibit cellular growth and complex I-derived OCR (0.7 µM MMe or 3 µM pCF_3-MMe). Levels of ATP were significantly reduced in both MMe and pCF_3-MMe treated cells, consistent with the inhibition of metabolic respiration (Figure 4E). Cells, including cancer cells, must maintain a high ATP:ADP ratio to maintain cellular functions and survival.[34] Moreover, AMP levels rise whenever the ATP:ADP ratio decreases, and an increase in the AMP:ATP ratio signals an energetic crisis in the cell. This energetic crisis is sensed by the master regulator AMP-Activated Protein Kinase (AMPK), which is activated through Thr172 phosphorylation and controls many signaling pathways ranging from energy metabolism to cellular growth.[34] Therefore, we evaluated if the reduction in ATP levels induced by MMe or pCF_3-MMe is sufficient to activate AMPK. KPC1242 cells treated with 0.7 µM MMe or 3 µM pCF_3-MMe, previously demonstrated to decrease ATP levels (Figure 4E), showed a significant increase in AMPK activation as quantified by increased Thr172 phosphorylation (Figures 4F and 4G).

Detection of pCF_3-MMe *in vitro* and *in vivo*

As natural organic compounds containing fluorine are rare in living organisms, we specifically chose tri-fluoromethyl groups when designing next-generation MMe analogs.[35] We aimed to leverage the nine
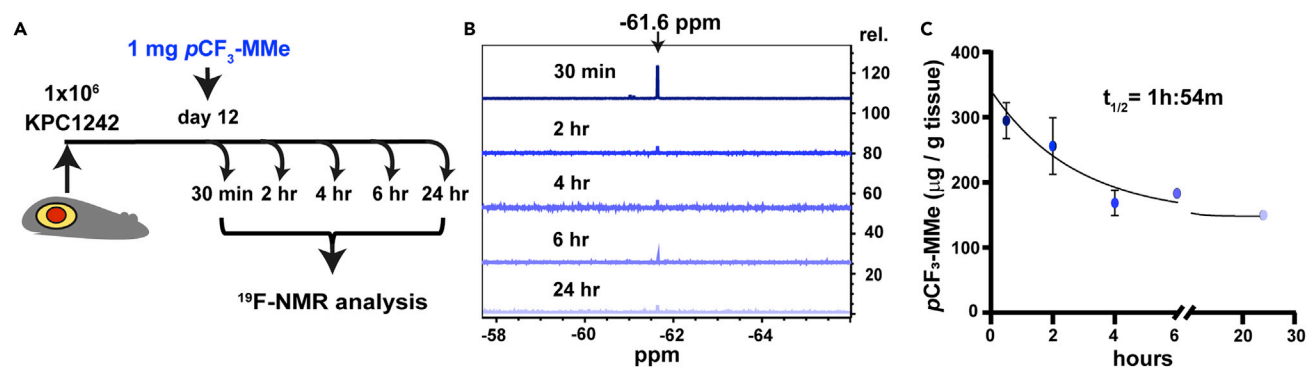
Figure 5. Quantification of pCF_3-MMe persistence within the tumor microenvironment

(A) Tumor engraftment and treatment schedule. KPC1242 murine pancreatic cancer engrafted mice were treated with an intra-tumoral injection of 1 mg pCF_3-MMe.

(B) Following treatment, pCF_3-MMe was extracted using 8:2 MeOH:H_2O at 30 min, 2, 4, 6, or 24 h and levels of pCF_3-MMe at each time point were quantified using quantitative NMR.

(C) Nonlinear fit curve analysis of pCF_3-MMe levels was used to generate $t_{1/2}$. Values are mean $\pm$ SEM from 1 to 4 biological replicates.

chemically equivalent fluorine atoms in the trifluoromethyl groups of pCF_3-MMe using ^{19}F-NMR. To detect cellular accumulation of pCF_3-MMe *in vitro*, KPC1242 cells were incubated with 1 mg pCF_3-MMe or vehicle (DMSO) in growth media for 2 h, followed by the removal of the media, compound extraction, and NMR analysis (Figure S7A). Four extraction conditions were tested: 8:2 MeOH:H_2O, 9:1 CHCl$_3$:MeOH, CH$_2$Cl$_2$, and 1:1 MeCN:H_2O. MeOH:H_2O (8:2) provided the most efficient extraction, evidenced by the strongest signal observed in ^{19}F-NMR (−61.6 ppm) among all tested conditions (Figures S7B–S7E). An additional peak was observed at −73.4 ppm in both the vehicle and pCF_3-MMe treated groups that likely originated from tissue culture plastics as removing the fluorinated plasti-cizer-containing research consumables completely abolished the signal (Figures S7not shown). To assess *in vivo* detection of pCF_3-MMe, mice engrafted with KPC1242 cells were administered 1 mg/mouse pCF_3-MMe for 2 h, followed by tumor harvest and compound extraction (Figure S8A). NMR analysis demonstrated the consistent detection of pCF_3-MMe, albeit with slightly different efficacy for each of the organic solvents tested (Figure S8). Much like extraction from cell culture, 8:2 MeOH:H_2O extraction was the most efficient for tissues (Figures S8B–S8E).

To validate ^{19}F-NMR as a viable detection approach, we analyzed the persistence of pCF_3-MMe in tumors. KPC1242 engrafted mice were administered 1 mg/mouse pCF_3-MMe starting 12 days after implantation. Mice were sacrificed, and tumors were extracted with 8:2 MeOH:H_2O 30 min, 2, 4, 6, or 24 h after treatment (Figure 5A). ^{19}F-NMR revealed measurable levels of pCF_3-MMe within the tumors 24 h after injection (Figure 5B). We next designed a quantitative NMR approach to measure the *in vivo* persistence of pCF_3-MMe. First, serial dilutions of known concentrations of pCF_3-MMe were prepared, and the intensity of the NMR peaks at a set scan number (n = 64) was used to create a standard curve. Next, a one-phase decay least-squares fit equation was generated to calculate the amount of pCF_3-MMe at each time point using the stan-dardized scan number. Nonlinear fit curve analysis revealed that pCF_3-MMe had a $t_{1/2}$ of 1.9 h (114 min) (Figure 5C). As an initial study of its pharmacodynamics, quantitative ^{19}F-NMR indicated that pCF_3-MMe was undetectable in the blood and liver 2 h after injection (Figure S9) and was barely detectable above the signal-to-noise ratio at 6 h (not shown). Taken together, these data reveal that the modification to TPP$^+$, particularly by adding chemically equivalent trifluoromethyl groups, allows ease of detection and monitoring of TPP$^+$-conjugated compounds.

pCF_3-MMe attenuates tumor progression *in vivo* with superior tolerability to mito-metformin

With the ability to detect pCF_3-MMe *in vitro* and *in vivo* in hand, along with anti-tumor properties and decreased toxicity toward non-transformed cells in culture, we next compared the tolerability of pCF_3-MMe in mice. Non-tumor-bearing mice received an intra-peritoneal injection with decreasing amounts (1 mg, 250, 100, 50, or 25 µg) of unsubstituted MMe or pCF_3-MMe. Additional mice were treated with 1 mg/mouse metformin as a treatment control (Figure 6A). Surprisingly, a single intra-peritoneal injection of 250 µg or 1 mg MMe to non-tumor-bearing mice resulted in significant and rapid mortality (Figures 6B and 6C). In stark contrast, pCF_3-MMe demonstrated vastly superior tolerability, with 100% of mice injected
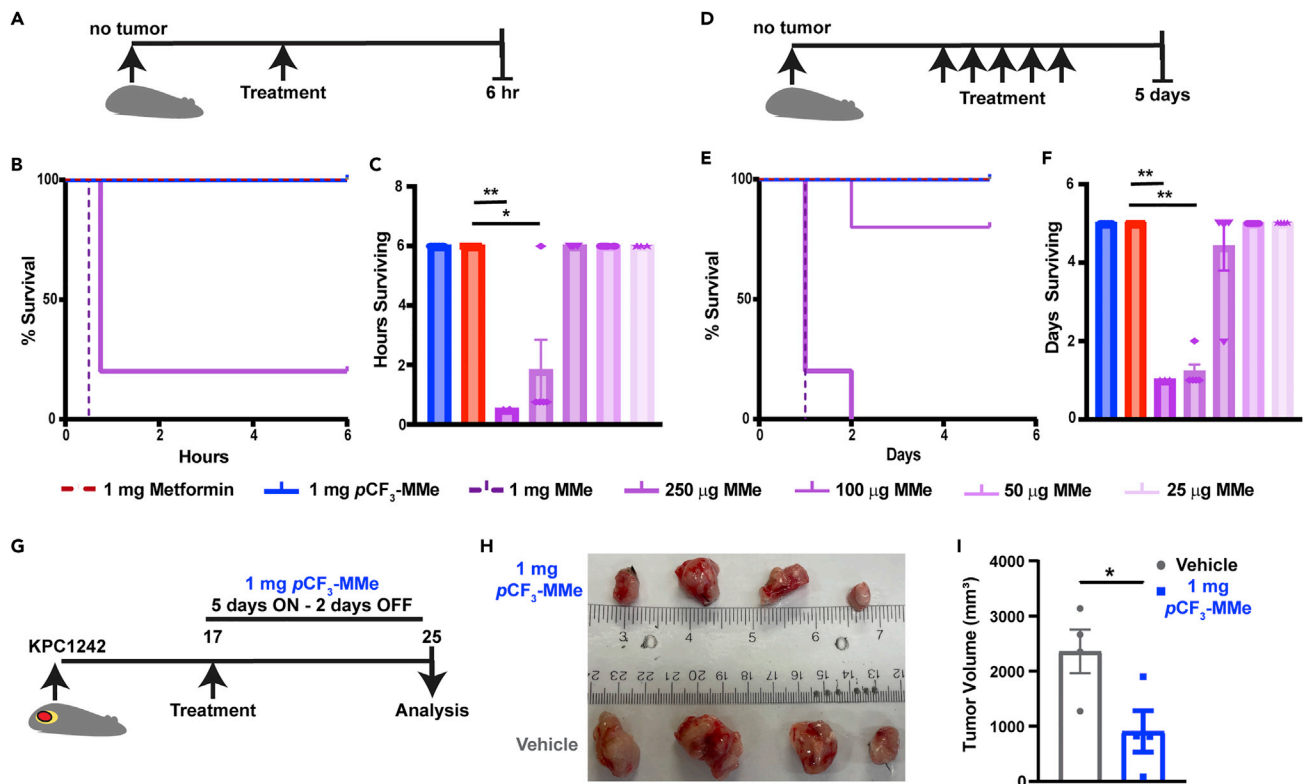
Figure 6. *p*CF₃-MMe inhibits tumor growth with enhanced biosafety relative to MMe

(A–I) C57BL/6J mice were treated with 1 mg MMe, 1 mg pCF$_3$-MMe, 1 mg MMe, 250 μg MMe, 100 μg MMe, 50 μg MMe, or 25 μg MMe for 6 h (A) or 5 days (D). Kaplan-Meier survival curve of mice treated for 6 h (B) or 5 days (E), n = 3-5. Numbers of mice surviving over time after a single injection (C) or 5 repeated doses (F). Significance was determined using a Mantel-Cox test (*, p < 0.05; **, p < 0.01). KPC1242 murine pancreatic cancer engrafted mice were treated with 1 mg pCF$_3$-MMe or vehicle 5 days on and 2 days off (G). Tumors isolated from vehicle and treated mice were pictured (H). Tumor volume was measured *ex vivo* from vehicle and pCF$_3$-MMe-treated mice (I). Values are mean ± SD. Significant differences were determined by Student's *t*-test (*, p < 0.05).

with 1 mg of the fluorinated analog surviving (Figures 6B and 6C). Metformin demonstrated a similar safety profile as pCF$_3$-MMe.

Given the strong safety shown from a single injection, we next determined if mice tolerated repeated injection using our published treatment schedule by injecting non-tumor-bearing mice daily for 5 consecutive days with doses ranging from as little as 25 μg/mouse to as much as 1 mg/mouse[20] (Figure 6D). Survival curves indicate that while each of the treated mice tolerated a 1 mg dose of pCF$_3$-MMe, parallel groups succumbed to 4-fold lower doses of un-fluorinated MMe (Figures 6E and 6F). Having shown that 1 mg/ mouse pCF$_3$-MMe was well tolerated in tumor-free animals, we next tested if pCF$_3$-MMe could inhibit tumor growth *in vivo*. Mice were implanted with murine cancer cells and injected 17 days after engraftment with 1 mg/mouse pCF$_3$-MMe (Figure 6G). Consistent with its anti-proliferative effects in culture, pCF$_3$-MMe significantly decreased tumor size and volume (Figures 6H and 6I). Taken together, trifluoromethylation of TPP$^+$ improves the reproducible detection, quantitative measurement, and safety profile of TPP$^+$-conjugated agents while retaining potent anti-tumor effects *in vivo*.

DISCUSSION

Cancer cell mitochondrial dysfunction and resulting membrane hyperpolarization have previously been exploited to study and deliver diagnostic and therapeutic agents.[1,17,18,30,36] While no underlying mechanism has been identified, this property is routinely exploited to selectively detect and target cancer *in vitro* and *in vivo*.[1,8–12,17–20,30,36,37] TPP$^+$-conjugated agents take advantage of this hyperpolarization to accumulate in cancer cells and have shown the most promising results in preclinical testing. However, early drug development efforts using TPP$^+$ have focused on modifying the aliphatic linker or the cargo.[12,19] Moreover, the development of TPP$^+$-conjugated compounds has been hindered by the lack of sensitive and unbiased

approaches to easily detect TPP$^+$-conjugated compounds and monitor their distribution in animal models.[12] Herein, TPP$^+$-conjugated MMe was rationally redesigned by directly modifying the TPP$^+$ moiety to enhance the partial positive charge on the phosphorus atom of the TPP$^+$ moiety. Using cell culture and preclinical models, we demonstrate that trifluoromethyl-modified MMe has improved selectivity and tolerability with the added benefit of sensitive and quantitative detection of fluorinated MMe *in vivo*. These data illustrate that harnessing the electron density of the phosphorus atom in the TPP$^+$ provides novel insight into the biological effects of modifying the TPP$^+$ moiety.

The large ionic radius of the unsubstituted TPP$^+$, mainly due to the delocalized cationic charge on the phosphorus atom, likely plays a role in the ability of TPP$^+$ to cross the cellular membrane and target the more negative inside membrane potential of mitochondria.[17] Thus, any substitution on the aryl rings of TPP$^+$ will likely impact the ability of these compounds to penetrate the membrane of cancer cells successfully and selectively.[17] A previous report investigated some of the chemical properties of aryl substitution on TPP$^+$, lacking the aliphatic carbon chain linker and a cargo, on normal non-transformed C2C12 myoblast cells.[21] However, gaps in this report included examining the roles of TPP$^+$ aryl substitution on the anti-tumor efficacy when a functional cargo is attached and assessing the preclinical potential of aryl-substituted TPP$^+$ compounds. Here, we modified the three TPP$^+$ aryl rings to determine if we could improve the mitochondrial localization and detectability of these reagents. The three novel compounds described, *p*CF$_3$-MMe, *m*CF$_3$-MMe, and *p*MeO-MMe, had distinct anti-tumor properties. The addition of trifluoromethyl groups in the *para* position on the TPP$^+$ moiety, *p*CF$_3$-MMe, was the most optimal modification, with only a slight change in efficacy compared to MMe in several types of cancer. Interestingly, the strongest effect was observed in cell selectivity, with *p*CF$_3$-MMe and *m*CF$_3$-MMe demonstrating a nearly 10-fold reduction in toxicity to normal cells compared to MMe. These data are consistent with a prior report demonstrating that *p*CF$_3$-TPP$^+$, a molecule lacking the aliphatic carbon chain linker and bioactive cargo, had no impact on OCR or proliferation of a non-transformed murine myoblast cell line.[21] In contrast to the fluorinated compound, *p*MeO-MMe exhibited lower efficacy in pancreas cancer cells, a diminishment we speculate reflects superior selectivity of *p*CF$_3$-MMe toward cancer cells, compared to the electron-donating methoxy groups in *p*MeO-MMe. Alternatively, the differences in the IC$_{50}$ curves between individual TPP-modified compounds or between the varying cancer cell lines may reflect the ability of each compound to activate discrete cellular pathways in different types of cancer cells. Indeed, we have previously shown that shortening the carbon linker between TPP and the bioactive moiety modulates the inhibitory effect of mitochondria-targeted agents.[38,39]

Fine-tuning the TPP$^+$ aryl rings with trifluoromethyl substituents increased lipophilicity while methoxy decreased lipophilicity as measured by the octanol/water partition coefficient (cLogP) *p*CF$_3$-MMe. These data suggest a potential mechanism for *p*CF$_3$-MMe's improved ability to cross the lipid bilayer and preferentially accumulate in mitochondria membranes. The increase in the partition coefficient of the lipophilic cation may be associated with a greater accumulation of the compound on the matrix side of mitochondria, consistent with the decreased retention of TMRE in *p*CF$_3$-MMe, relative to *p*MeO-MMe, treated cells. While the ratio of the membrane-bound and unbound pools of the compound is defined by the partition constant, the total accumulation at equilibrium is heavily controlled by the membrane potential, as predicted by the Nernst equation, with correction due to membrane/cytosol or matrix partitioning. Thus, changes in the partition coefficient and the electron density may work cooperatively to enhance *p*CF$_3$-MMe selectivity toward cancer cells.

The mechanism of action of *p*CF$_3$-MMe remained intact relative to the unsubstituted MMe. As shown for the parental compound and several other TPP$^+$-conjugated compounds, *p*CF$_3$-MMe decreased mitochondrial respiration, inhibited complex I, decreased ATP levels, and activated AMPK signaling in a concentration-dependent manner.[8–12,19,20,37] These data indicate the *para* trifluoromethyl substitution did not impact critical binding interactions or decrease the activity of the parent molecule. Importantly, while the *para* trifluoromethyl aryl substitutions did not interfere with the mechanism of action, this substitution improved the selectivity and tolerability of the molecules *in vitro* and *in vivo*. This partly reflects the increase in partial positive charge on the phosphorus atom of *p*CF$_3$-MMe, which suggests better accumulation within tumor cells. Kulkarni and colleagues showed that using a *p*CF$_3$-TPP$^+$ substituted on the phenyl rings, in the absence of any conjugated cargo, did not prevent the modified TPP$^+$ moiety from accumulating within the mitochondria of intact cells. Indeed, *para*-substitution of the TPP$^+$ phenyl rings led to a higher mitochondrial accumulation of cargo than that mediated by unmodified TPP$^+$.[21] Combined, these data

demonstrate that the pCF_3-TPP$^+$ moiety is a very promising lead for developing mitochondria-targeting agents with increased safety profiles. Our results support those findings with the increased benefit that adding the bioactive cargo metformin to generate pCF_3-MMe retained strong inhibitory effects on mitochondrial respiration. These data suggest that the metformin cargo conjugated to pCF_3-TPP provided anti-proliferative impact on cancer cells.

Cumulatively, pCF_3-MMe has significant other advantages over traditional unsubstituted TPP$^+$-conjugated compounds. First, the detection of pCF_3-MMe using ^{19}F-NMR is greatly enhanced *in vitro* and *in vivo*. The ability to quantitative measurement via ^{19}F-NMR is a marked improvement on the traditional detection of unsubstituted TPP$^+$-conjugated compounds requiring a laborious process for detection using LC/MS requiring unique method development for each compound synthesized. Using ^{19}F-NMR, the half-life of pCF_3-MMe was determined to be ∼2 h, a level that closely resembles the pharmacodynamics of many anti-cancer agents.[40] The inability to detect pCF_3-MMe in the blood and liver at 30 -minutes or 6 h supports the idea that the compound is retained at the injection site. A caveat to that interpretation is that metformin is not metabolized and is instead excreted as an intact molecule in the urine.[41] While reports suggest metformin has a half-life of ∼5 h, the compound is poorly absorbed, with large inter-individual variability in pharmacokinetics.[42] In contrast to pCF_3-MMe, pharmacokinetic and pharmacodynamic studies of MitoQ, a different, non-fluorinated, TPP$^+$-conjugated compound, revealed rapid uptake followed by a sharp decline in the compound after administration, with a half-life of ∼30 min, with the molecule being excreted as an intact molecule in the urine.[43] Yet another advantage is that pCF_3-MMe demonstrated a significantly improved safety profile *in vivo* similar, with the fluorinated compound demonstrating comparable potency to the FDA-approved parent drug metformin. While additional studies are needed to evaluate the pharmacokinetics, pharmacodynamics, and safety profile of TPP$^+$-conjugated metformin analogs, the work herein demonstrate that these newly designed compounds may be useful in completing rigorous pharmacology studies. Moreover, pCF_3-MMe opens the door for the non-invasive monitoring of pCF_3-TPP$^+$ compounds with complementary techniques such as ^{19}F-MRI and ^{18}F-PET.

Limitations of the study

Our data indicate that TPP$^+$-modified variants of MMe retain anti-tumor effects on cancer cell growth and mitochondrial respiration. While we demonstrated strong sensitivity for *in vivo* and *in vitro* detection using NMR spectroscopy, ^{18}F positron emission tomography or other reliable approaches for *in vivo* quantification remain to be optimized. Similarly, the detection and quantification of fluorinated MMe variants within the heterogeneous cell populations of solid tumors have yet to be completed. Those studies would facilitate the validation of tumor selectivity by TPP$^+$-modified compounds. Further chemical modifications, including fluorination at the *ortho*-carbon position, or saturation with additional fluorines have yet to be synthesized and tested.

STAR★METHODS

Detailed methods are provided in the online version of this paper and include the following:

- KEY RESOURCES TABLE
- RESOURCE AVAILABILITY
  - Lead contact
  - Materials availability
  - Data and code availability
- EXPERIMENTAL MODEL DETAILS
  - Cell culture
  - Animal models
- METHOD DETAILS
  - Cell growth and proliferation
  - Extracellular flux
  - ATP measurements
  - Immunoblotting
  - Sample preparation and NMR analysis
  - NMR data collection
  - Electron density calculations
  - General compound synthesis methods and equipment

SUPPLEMENTAL INFORMATION

Supplemental information can be found online at https://doi.org/10.1016/j.isci.2022.105670.

AUTHOR CONTRIBUTIONS

Conceptualization: MAE, RFK, BCS, and MBD; formal analysis: MAE, RFK, DM, and FP; funding acquisition: BCS and MBD, investigation: MAE, RFK, and DM; methodology: MAE, RFK, BCS, and MBD; project administration: MBDResources: BCS, IPK, PC-R, FP, and MBD; supervision: BCS and MBD; validation: MAE, RFK, DM, and FP; visualization: MAE, RFK, DJS, DM, and MBD; writing – original draft: MAE; writing – review and editing: MAE, RFK, DJS, BCS, and MBD.

DECLARATION OF INTERESTS

MBD and FP are co-founders and have ownership and financial interests in Protein Foundry, LLC and Xlock Biosciences, LLC. Chemical modifications of mitochondria-targeted compounds, including those included in this report, are covered by a provisional US Patent, U.S. Application No. 63/285,374, to MBD, BCS, MAE, and RK. The remaining authors have no competing interests to disclose.

INCLUSION AND DIVERSITY

We support inclusive, diverse, and equitable conduct of research. One or more of the authors of this paper self-identifies as an underrepresented ethnic minority in their field of research or within their geographical location. One or more of the authors of this paper self-identifies as living with a disability.

REFERENCES

1. Smith, R.A.J., Porteous, C.M., Gane, A.M., and Murphy, M.P. (2003). Delivery of bioactive molecules to mitochondria in vivo. Proc. Natl. Acad. Sci. USA 100, 5407–5412. https://doi.org/10.1073/pnas.0931245100.

2. Frattaruolo, L., Brindisi, M., Curcio, R., Marra, F., Dolce, V., and Cappello, A.R. (2020). Targeting the mitochondrial metabolic network: a promising strategy in cancer treatment. Int. J. Mol. Sci. 21, 6014. https://doi.org/10.3390/ijms21176014.

3. Rovini, A., Heslop, K., Hunt, E.G., Morris, M.E., Fang, D., Gooz, M., Gerencser, A.A., and Maldonado, E.N. (2021). Quantitative analysis of mitochondrial membrane potential heterogeneity in unsynchronized and synchronized cancer cells. FASEB J. 35, e21148. https://doi.org/10.1096/fj.202001693R.

4. Momcilovic, M., Jones, A., Bailey, S.T., Waldmann, C.M., Li, R., Lee, J.T., Abdelhady, G., Gomez, A., Holloway, T., Schmid, E., et al. (2019). In vivo imaging of mitochondrial membrane potential in non-small-cell lung cancer. Nature 575, 380–384. https://doi.org/10.1038/s41586-41019-41715-41580.

5. Armstrong, J.S. (2007). Mitochondrial medicine: pharmacological targeting of mitochondria in disease. Br. J. Pharmacol. 151, 1154–1165. https://doi.org/10.1038/sj.bjp.0707288.

6. Zong, W.X., Rabinowitz, J.D., and White, E. (2016). Mitochondria and cancer. Mol. Cell 61, 667–676. https://doi.org/10.1016/j.molcel.2016.1002.1011.

7. Pustylnikov, S., Costabile, F., Beghi, S., and Facciabene, A. (2018). Targeting mitochondria in cancer: current concepts and immunotherapy approaches. Transl. Res. 202, 35–51. https://doi.org/10.1016/j.trsl.2018.1007.1013.

8. Cheng, G., Zielonka, J., Dranka, B.P., McAllister, D., Mackinnon, A.C., Jr., Joseph, J., and Kalyanaraman, B. (2012). Mitochondria-targeted drugs synergize with 2-deoxyglucose to trigger breast cancer cell death. Cancer Res. 72, 2634–2644. https://doi.org/10.1158/0008-5472.CAN-11-3928.

9. Cheng, G., Zielonka, J., Ouari, O., Lopez, M., McAllister, D., Boyle, K., Barrios, C.S., Weber, J.J., Johnson, B.D., Hardy, M., et al. (2016). Mitochondria-targeted analogues of metformin exhibit enhanced antiproliferative and radiosensitizing effects in pancreatic cancer cells. Cancer Res. 76, 3904–3915. https://doi.org/10.1158/0008-5472.CAN-15-2534.

10. Cheng, G., Zielonka, J., Hardy, M., Ouari, O., Chitambar, C.R., Dwinell, M.B., and Kalyanaraman, B. (2019). Synergistic inhibition of tumor cell proliferation by metformin and mito-metformin in the presence of iron chelators. Oncotarget 10, 3518–3532. https://doi.org/10.18632/oncotarget.26943.

11. Boyle, K.A., Van Wickle, J., Hill, R.B., Marchese, A., Kalyanaraman, B., and Dwinell, M.B. (2018). Mitochondria-targeted drugs stimulate mitophagy and abrogate colon cancer cell proliferation. J. Biol. Chem. 293, 14891–14904. https://doi.org/10.1074/jbc.RA117.001469.

12. Zielonka, J., Joseph, J., Sikora, A., Hardy, M., Ouari, O., Vasquez-Vivar, J., Cheng, G., Lopez, M., and Kalyanaraman, B. (2017). Mitochondria-targeted triphenylphosphonium-based compounds: syntheses, mechanisms of action, and therapeutic and diagnostic applications. Chem. Rev. 117, 10043–10120. https://doi.org/10.1021/acs.chemrev.7b00042.

13. Kalyanaraman, B., Cheng, G., Hardy, M., Ouari, O., Lopez, M., Joseph, J., Zielonka, J., and Dwinell, M.B. (2018). A review of the basics of mitochondrial bioenergetics, metabolism, and related signaling pathways in cancer cells: therapeutic targeting of tumor mitochondria with lipophilic cationic compounds. Redox Biol. 14, 316–327. https://doi.org/10.1016/j.redox.2017.09.020.

14. Murphy, J.W., Cho, Y., Sachpatzidis, A., Fan, C., Hodsdon, M.E., and Lolis, E. (2007). Structural and functional basis of CXCL12 (stromal cell-derived factor-1 alpha) binding to heparin. J. Biol. Chem. 282, 10018–10027. https://doi.org/10.1074/jbc.M608796200.

15. Ross, M.F., Prime, T.A., Abakumova, I., James, A.M., Porteous, C.M., Smith, R.A.J., and Murphy, M.P. (2008). Rapid and extensive uptake and activation of hydrophobic triphenylphosphonium cations within cells. Biochem. J. 411, 633–645. https://doi.org/10.1042/BJ20080063.

16. Hanahan, D., and Weinberg, R.A. (2011). Hallmarks of cancer: the next generation. Cell 144, 646–674. https://doi.org/10.1016/j.cell.2011.02.013.

17. Murphy, M.P. (1997). Selective targeting of bioactive compounds to mitochondria. Trends Biotechnol. 15, 326–330. https://doi.org/10.1016/S0167-7799(1097)01068-01068.

18. Jauslin, M.L., Meier, T., Smith, R.A.J., and Murphy, M.P. (2003). Mitochondria-targeted antioxidants protect Friedreich Ataxia fibroblasts from endogenous oxidative stress more effectively than untargeted antioxidants. FASEB J. 17, 1972–1974. https://doi.org/10.1096/fj.1903-0240fje.

19. Cheng, G., Hardy, M., Topchyan, P., Zander, R., Volberding, P., Cui, W., and Kalyanaraman, B. (2020). Potent inhibition of tumour cell proliferation and immunoregulatory function by mitochondria-targeted atovaquone. Sci. Rep. 10, 17872. https://doi.org/10.11038/s41598-17020-74808-17870.

20. AbuEid, M., McAllister, D.M., McOlash, L., Harwig, M.C., Cheng, G., Drouillard, D., Boyle, K.A., Hardy, M., Zielonka, J., Johnson, B.D., et al. (2021). Synchronous effects of targeted mitochondrial complex I inhibitors on tumor and immune cells abrogate melanoma progression. iScience 24, 102653. https://doi.org/10.101016/j.isci.102021.102653. eCollection 102021 Jun 102625.

21. Kulkarni, C.A., Fink, B.D., Gibbs, B.E., Chheda, P.R., Wu, M., Sivitz, W.I., and Kerns, R.J. (2021). A novel triphenylphosphonium carrier to target mitochondria without uncoupling oxidative phosphorylation. J. Med. Chem. 64, 662–676. https://doi.org/10.1021/acs.jmedchem.1020c01671.

22. Meanwell, N.A. (2018). Fluorine and fluorinated motifs in the design and application of bioisosteres for drug design. J. Med. Chem. 61, 5822–5880. https://doi.org/10.1021/acs.jmedchem.5827b01788.

23. Alvarez, S. (2013). A cartography of the van der Waals territories. Dalton Trans. 42, 8617–8636. https://doi.org/10.1039/c8613dt50599e. Epub 52013 May 50591.

24. Inoue, M., Sumii, Y., and Shibata, N. (2020). Contribution of organofluorine compounds to pharmaceuticals. ACS Omega 5, 10633–10640. https://doi.org/10.11021/acsomega.10630c00830.

25. Wilson, D.F. (2017). Oxidative phosphorylation: regulation and role in cellular and tissue metabolism. J. Physiol. 595, 7023–7038. https://doi.org/10.1113/JP273839.

26. Plitzko, B., and Loesgen, S. (2018). Measurement of oxygen consumption rate (OCR) and extracellular acidification rate (ECAR) in culture cells for assessment of the energy metabolism. Bio. Protoc. 8, e2850. https://doi.org/10.21769/BioProtoc.22850.

27. Ehinger, J.K., Piel, S., Ford, R., Karlsson, M., Sjövall, F., Frostner, E.Å., Morota, S., Taylor, R.W., Turnbull, D.M., Cornell, C., et al. (2016). Cell-permeable succinate prodrugs bypass mitochondrial complex I deficiency. Nat. Commun. 7, 12317. https://doi.org/10.1038/ncomms12317.

28. Piel, S., Ehinger, J.K., Chamkha, I., Frostner, E.Å., Sjövall, F., Elmér, E., and Hansson, M.J. (2018). Bioenergetic bypass using cell-permeable succinate, but not methylene blue, attenuates metformin-induced lactate production. Intensive Care Med. Exp. 6, 22. https://doi.org/10.1186/s40635-40018-40186-40631.

29. Callahan, J., and Kopecek, J. (2006). Semitelechelic HPMA copolymers functionalized with triphenylphosphonium as drug carriers for membrane transduction and mitochondrial localization. Biomacromolecules 7, 2347–2356. https://doi.org/10.1021/bm060336m.

30. Kelso, G.F., Porteous, C.M., Coulter, C.V., Hughes, G., Porteous, W.K., Ledgerwood, E.C., Smith, R.A., and Murphy, M.P. (2001). Selective targeting of a redox-active ubiquinone to mitochondria within cells: antioxidant and antiapoptotic properties. J. Biol. Chem. 276, 4588–4596. https://doi.org/10.1074/jbc.M009093200.

31. Scaduto, R.C., Jr., and Grotyohann, L.W. (1999). Measurement of mitochondrial membrane potential using fluorescent rhodamine derivatives. Biophys. J. 76,

469–477. https://doi.org/10.1016/S0006-3495(1099)77214-77210.

32. Bernas, T., and Dobrucki, J. (2002). Mitochondrial and nonmitochondrial reduction of MTT: interaction of MTT with TMRE, JC-1, and NAO mitochondrial fluorescent probes. Cytometry *47*, 236–242. https://doi.org/10.1002/cyto.10080.

33. Seyfried, T.N., Arismendi-Morillo, G., Mukherjee, P., and Chinopoulos, C. (2020). On the origin of ATP synthesis in cancer. iScience *23*, 101761. https://doi.org/10.101016/j.isci.102020.101761.

34. Herzig, S., and Shaw, R.J. (2018). AMPK: guardian of metabolism and mitochondrial homeostasis. Nat. Rev. Mol. Cell Biol. *19*, 121–135. https://doi.org/10.1038/nrm.2017.1095.

35. Thuronyi, B.W., Privalsky, T.M., and Chang, M.C.Y. (2017). Engineered fluorine metabolism and fluoropolymer production in living cells. Angew. Chem. Int. Ed. *56*, 13637–13640. https://doi.org/10.11002/anie.201706696.

36. Buskiewicz, I.A., Montgomery, T., Yasewicz, E.C., Huber, S.A., Murphy, M.P., Hartley, R.C., Kelly, R., Crow, M.K., Perl, A., Budd, R.C., and Koenig, A. (2016). Reactive oxygen species induce virus-independent MAVS oligomerization in systemic lupus erythematosus. Sci. Signal. *9*, ra115. https://doi.org/10.1126/scisignal.aaf1933.

37. Cheng, G., Zielonka, J., McAllister, D., Hardy, M., Ouari, O., Joseph, J., Dwinell, M.B., and Kalyanaraman, B. (2015). Antiproliferative effects of mitochondria-targeted cationic antioxidants and analogs: role of mitochondrial bioenergetics and energy-sensing mechanism. Cancer Lett. *365*, 96–106. https://doi.org/10.1016/j.canlet.2015.05.016.

38. Cheng, G., Hardy, M., Zielonka, J., Weh, K., Zielonka, M., Boyle, K.A., Abu Eid, M., McAllister, D., Bennett, B., Kresty, L.A., et al. (2020). Mitochondria-targeted magnolol inhibits OXPHOS, proliferation, and tumor growth via modulation of energetics and autophagy in melanoma cells. Cancer Treat. Res. Commun. *25*, 100210. https://doi.org/10.1016/j.ctarc.2020.100210.

39. Cheng, G., Hardy, M., Topchyan, P., Zander, R., Volberding, P., Cui, W., and Kalyanaraman, B. (2021). Mitochondria-targeted hydroxyurea inhibits OXPHOS and induces antiproliferative and immunomodulatory effects. iScience *24*, 102673. https://doi.org/10.101016/j.isci.102021.102673.

40. Rodríguez-Gascón, A., Solinís, M.Á., and Isla, A. (2021). The role of PK/PD analysis in the development and evaluation of antimicrobials. Pharmaceutics *13*, 833. https://doi.org/10.3390/pharmaceutics13060833.

41. McCreight, L.J., Bailey, C.J., and Pearson, E.R. (2016). Metformin and the gastrointestinal tract. Diabetologia *59*,

426–435. https://doi.org/10.1007/s00125-00015-03844-00129.

42. Graham, G.G., Punt, J., Arora, M., Day, R.O., Doogue, M.P., Duong, J.K., Furlong, T.J., Greenfield, J.R., Greenup, L.C., Kirkpatrick, C.M., et al. (2011). Clinical pharmacokinetics of metformin. Clin. Pharmacokinet. *50*, 81–98. https://doi.org/10.2165/11534750-000000000-000000000.

43. Smith, R.A.J., and Murphy, M.P. (2010). Animal and human studies with the mitochondria-targeted antioxidant MitoQ. Ann. N. Y. Acad. Sci. *1201*, 96–103. https://doi.org/10.1111/j.1749-6632.2010.05627.x.

44. Hwang, R.F., Moore, T., Arumugam, T., Ramachandran, V., Amos, K.D., Rivera, A., Ji, B., Evans, D.B., and Logsdon, C.D. (2008). Cancer-associated stromal fibroblasts promote pancreatic tumor progression. Cancer Res. *68*, 918–926. https://doi.org/10.1158/0008-5472.CAN-07-5714.

45. Herrera, D., Peral, D., and Bayón, J.C. (2022). Preparation of carboxylic arylphosphines by hydrolysis of the trifluoromethyl group. RSC Adv. *12*, 7103–7114. https://doi.org/10.1039/d7102ra00420h.

46. Fortun, S., and Schmitzer, A.R. (2018). Synthesis and characterization of biguanide and biguanidium surfactants for efficient and recyclable application in the suzuki-miyaura reaction. ACS Omega *3*, 1889–1896. https://doi.org/10.1021/acsomega.1887b01962.

STAR★METHODS

KEY RESOURCES TABLE

REAGENT or RESOURCE	SOURCE	IDENTIFIER
Antibodies		
FITC-conjugated monoclonal anti-Ki-67 (SolA15)	ThermoFisher	RRID: AB-11151330
Rabbit anti-phospho-AMPKalpha	Cell Signaling Technologies	RRID:AB-330330
Rabbit anti-total-AMPKalpha	Cell Signaling Technologies	RRID:AB-330331
HRP-conjugated rabbit IgG	Cytiva, Amersham	RRID:AB-772191
Chemicals, peptides, and recombinant proteins		
DMEM	Gibco Life Technologies	Cat# 11965084
RPMI 1640 Medium	Gibco Technologies	Cat# 11875119
McCoy's modified medium	Gibco Technologies	Cat# 16600082
Fetal bovine serum	Omega	Cat# FB-12
L-glutamine GlutaMAX	Gibco Technologies	Cat# 35050-061
D-glucose	Gibco Technologies	Cat# J60067.EQE
M3-Base A	Incell	Cat# M300F-500
Human EGF	Gibco	Cat# PHG0313
Puromycin	ThermoFisher	Cat# A1113802
Dulbecco's-modified PBS	Gibco Life Technologies	Cat# 14190
Paraformaldehyde	Sigma	Cat# 158127
Triton X-100	Fisher Scientific	Cat# 327371000
Oligomycin	Sigma	Cat# O4876
Dinitrophenol	Sigma	Cat# D198501
Rotenone	Sigma	Cat# R8875
Antimycin A	Sigma	Cat# A8674
Protease inhibitor cocktail set III	Millipore Sigma	Cat# 539134
Nonidet P-40	ThermoFisher	Cat# 28324
EDTA	Life Technologies	Cat# 15575-038
Sodium fluoride	Sigma	Cat# S-1504
SDS	ThermoFisher	Cat# BP166500
Sodium orthovanadate	Sigma	Cat# S6508
Beta-glycerol phosphate	Sigma	Cat#G9891
N-(10-bromodecyl)phthalimide	Combi-Blocks, Inc	Cat#QI-5596
anhydrous acetonitrile (CH3CN)	Sigma Aldrich	Cat # 271004
N,N-dimethylformamide (DMF)	Sigma Aldrich	Cat# 227056
methanol	Sigma Aldrich	Cat # 179337
Dichloromethane (DCM)	Sigma Aldrich	Cat #D65100
Triphenylphosphine	Oakwood	Cat # 037818
Tris(4-trifluoromethyl)phosphine	Ambeed	Cat # A108436
Tris(4-methoxyphenyl)phosphine	Ambeed	Cat # A354955
Ethanol	Decon Labs	Cat # UN1987
Hydrazine	Sigma Aldrich	Cat # 21555
Diethyl ether	Sigma Aldrich	Cat # 673811
n-butanol	Sigma Aldrich	Cat # 360465

Continued

REAGENT or RESOURCE	SOURCE	IDENTIFIER
HCl	Sigma Aldrich	Cat # 294837
cyanoguanidine	Sigma Aldrich	Cat #D76609
Critical commercial assays		
Luminescent ATP Detection Assay	Abcam	Cat# ab113849
Experimental models: Cell lines		
Panc-1	ATCC	RRID:CVCL-0480
MDA-MB-231	ATCC	RRID:CVCL-0062
AsPC1	ATCC	RRID:CVCL-0152
OVCAR-8	ATCC	RRID:CVCL-1629
OVCAR-4	ATCC	RRID:CVCL-1627
HCT-116	ATCC	RRID:CVCL-0291
HPNE	ATCC	RRID:CVCL-C466
KPC1242	David Tuveson	
HPSC	Rosa Hwang	PMCID: PMC2519173
Experimental models: Organisms/strains		
C57BL/6J	The Jackson Laboratories	RRID:IMSR-JAX:000,664
Software and algorithms		
GraphPad Prism v.9.2.0	GraphPad Software, San Diego, CA	RRID:SCR_002798
Alpha View Software v.3.5.0	Protein Simple, Santa Clara, CA	
Schrodinger Computational Suite v.2021-1		RRID:SCR_014879
ChemDraw Professional 18.0	PerkinElmer	https://www.perkinelmer.com/category/chemdraw

RESOURCE AVAILABILITY

Lead contact

Further information and requests for resources and reagents should be directed to and will be fulfilled by the lead contact, Dr. Michael Dwinell (mdwinell@mcw.edu).

Materials availability

Chemical modifications of mitochondria-targeted compounds, including those included in this report, are covered by a provisional patent [U.S. Application No. 63/285,374].

Compounds generated in this work will be provided following the completion of an institutional signed material transfer agreement.

Data and code availability

- All data reported in this paper will be shared by the lead contact upon request.

- This paper does not report original code.

- Any additional information required to reanalyze the data reported in this paper is available from the lead contact upon request.

EXPERIMENTAL MODEL DETAILS

Cell culture

Murine pancreatic cancer cells KPC1242 (David Tuveson, Cold Spring Harbor), human pancreatic cancer cells, Panc-1 (RRID:CVCL-0480), human breast cancer cells MDA-MB-231 (RRID:CVCL-0062), and human pancreatic stellate cells HPSC (Rosa F. Hwang, MD Anderson Cancer Center)[44] were all cultured in DMEM (Gibco ThermoFisher Scientific, Waltham, MA, Cat#11965084) containing 10% v/v fetal bovine

serum (Omega Scientific, Inc., Tarzana, CA, Cat# FB-12). Human pancreatic cancer cells AsPC-1 (RRID:CVCL-0152), human ovarian cancer cells OVCAR-8 (RRID:CVCL-1629), and human ovarian cancer cells OVCAR-4 (RRID:CVCL-1627) were all cultured in RPMI media (Cat# 22400089) containing 10% v/v fetal bovine serum (Omega Scientific). Human colon cancer cells HCT-116 (RRID:CVCL-0291) were cultured in McCoy's 5A Modified Medium (Gibco, Cat# 16600082) containing 10% v/v fetal bovine serum (Omega Scientific). Human pancreatic duct epithelial cells HPNE (RRID:CVCL-C466) were cultured in DMEM and 200 mM L-Glutamine and 7.5% w/v $NaCO_3$ further supplemented with 15% v/v fetal bovine serum, M3-Base A (Incell, San Antonio, TX), 1M D-Glucose (Gibco Cat#J60067.EQE), 100 μg/mL human EGF (Gibco Cat# PHG0313) and 10 mg/mL puromycin (ThermoFisher, Cat#A1113802).

Animal models

All animal studies were approved by the Institutional Animal Care and Use Committees at the Medical College of Wisconsin. C57BL/6J mice (RRID: IMSR JAX:000,664) were purchased from The Jackson Laboratory (Bar Harbor, ME). Six-to eight-week-old male or female mice were randomly assigned to treatment or control groups and implanted subcutaneously in the right flank with 1×10^6 KPC1242 murine pancreatic cancer cells. Tumors were allowed to establish for 12-17 days before intra-tumoral treatment. Mice were randomly assigned to control or experimental treatment groups immediately before treatment by an investigator blinded to the *ex vivo* tumor measurements. Treated tumor-bearing mice received a single injection of compound resuspended in Dulbecco's-modified PBS (Gibco Life Technologies, Cat#14190) in a final 50 μL volume directly to the tumor mass using a 1.5 mL syringe and 28-gauge × 0.5 cm needle (Franklin Lakes, NJ, Cat#329461). At study end tumors were excised, and volume (length × width × depth = mm^3) measured postmortem using calipers. Tumors were then fixed in zinc formalin and cleared in 70% v/v ethanol, embedded in paraffin, and 7 μm sections stained for immunohistochemical analysis.

METHOD DETAILS

Cell growth and proliferation

Cells were plated to standard 96-well tissue culture plates at 4,000 cells/well. Mitochondria-targeted compounds were diluted in full serum medium and added to wells. Cell confluence was measured using an IncuCyte S3 every 2 h at 10× magnification. To measure proliferation, KPC1242 cells (2×10^4) were treated with MMe or pCF$_3$-MMe for 24 h, fixed with 1% v/v PFA (Sigma, Cat#158127), permeabilized with 0.2% v/v Triton X-100 (Fisher, Cat# 327371000), and stained using FITC-conjugated Ki-67 antibody (ThermoFisher, Cat# 11-5698-82 [RRID: AB-11151330]). Image analyses were conducted using the IncuCyte S3 imaging software system.

Extracellular flux

Cells were plated to Seahorse XF96 cell culture microplates at 20,000 cells/well. Stock compounds in DMSO were diluted in RPMI (Gibco, Cat#11875119) medium to a final concentration in 100 mL volume, incubated at 37°C for 24 h, centrifuged at 200 × g for 2 min, and conditioned medium removed and replaced with serum-free RPMI (200 mL). Oxygen consumption rate (OCR) and extracellular acidification rate (ECAR) were measured after injections of 1 mg/mL oligomycin (Sigma, Cat# O4876), 50 mM dinitrophenol (Sigma, Cat# D198501), 1 mM rotenone (Sigma, Cat# R8875), and 10 mM antimycin A (Sigma, Cat# A8674). Analysis was performed by normalizing OCR and ECAR readouts to vehicle controls. Complex I and II activity were analyzed after permeabilization of the cells.

ATP measurements

KPC1242 cells (2×10^4) were treated with MMe or pCF$_3$-MMe for 24 h. Intracellular ATP levels were determined in cell lysates using a Luminescent ATP Detection Assay Kit per the manufacturer's directions (Abcam, Cambridge, UK, Cat# ab113849).

Immunoblotting

Cells were serum-starved for 24 h followed by compound treatment for 24 h before lysis in RIPA buffer composed of 50 mM Tris-HCl, pH 7.4, 150 mM NaCl, 0.25% v/v sodium deoxycholate, 1% v/v Nonidet P-40 (ThermoFisher, Cat#28324), 0.1% v/v SDS (Fisher, Cat#BP166500), 1 mM EDTA (Life Technologies, Cat#15575-038), 10 mM sodium orthovanadate (Sigma Cat#S6508), 40 mM β-glycerol phosphate (Sigma Cat# G9891), 20 mM sodium fluoride (Sigma, Cat#S1504), and protease inhibitors cocktail set III (Millipore Sigma, Cat#539134). Protein (10 μg) was loaded to each lane and separated by reducing SDS-PAGE. The

separated proteins were electro-transferred to PVDF membranes and incubated with primary anti-phospho-AMPKα or anti-total AMPKα (Cell Signaling Technology #2531S [RRID:AB_330330] or #2532S [RRID:AB_330331], respectively) or anti-β-actin (Cell Signaling, Cat# 4970S [RRID:AB_2223172]). Primary antibodies were detected by incubating with secondary horseradish peroxidase-conjugated antibody (Cytiva, Amersham ECL rabbit IgG-HRP, Cat# NA9340 [RRID:AB_772191]). Densitometric quantification of phosphorylated, total or actin protein levels was measured using chemiluminescence and calculated using Alpha View Software (ProteinSimple, Santa Clara, CA).

Sample preparation and NMR analysis

Cells (1×10^7 cells/10 cm dish) were allowed to adhere overnight and then treated with varying concentrations of mitochondria-targeted compounds. Compounds were extracted using multiple methods and optimized for detection and quantification: A) Cells or tumors were placed in a dry ice ethanol bath followed by 80% v/v MeOH in water. Cells were placed on a dry ice ethanol bath on an orbital shaker for 20 min, and then cells were collected and centrifuged at $10,000 \times g$; B) Post-treatment cells were lifted with TrypLE (Gibco, Cat# 11558856) and centrifuged, then compound was extracted from the cells or tumors with 9:1 $CHCl_3:H_2O$, CH_2Cl_2, or 1:1 $MeCN:H_2O$. Following extraction, solvents were evaporated using a Biotage V-10 Touch (Uppsala, Sweden), and before NMR acquisition, samples were resuspended in an equal volume of DMSO-d_6.

NMR data collection

^{19}F 1D-NMR spectra were collected on a Bruker Avance-III 500 MHz NMR spectrometer equipped with a $^1H\&^{19}F/^{13}C/^{15}N$–TCI cryoprobe. All ^{19}F data were collected at 25°C using a 1D pulse sequence with a 30° flip-angle, 64 transients, and an automatic receiver gain. TopSpin 3.6.1 was used to process all spectra and integrate the peak intensity corresponding to the pCF$_3$-MMe ^{19}F signal at −61.6 ppm. To evaluate pCF$_3$-MMe concentrations in biological samples, a standard curve was generated using pCF$_3$-MMe concentrations of 0.25, 0.50, 0.75, 1.0, 1.25, and 1.5 mg/mL, and the resulting peak intensities were analyzed by linear regression. The standard curve was then used to calculate the amount of pCF$_3$-MMe present per gram of tissue in the processed biological samples.

Electron density calculations

Computational calculations were performed with the Schrodinger Computational Suite v. 2021-1 (RRID:SCR_014879). Using the LigPrep workflow, all molecules were prepared in the OPLS4 force field at pH = 7. Using the Jaguar interface and default settings, electron density and electrostatic potential surfaces of the prepared molecules were calculated using B3LYP-D3 theory and the 6-31G** basis set. Color ramping (minimum and maximum) for the heatmap was normalized to unconjugated MMe.

General compound synthesis methods and equipment

All reagents and solvents were commercial grade and purified before use. Thin-layer chromatography was performed using glass-backed silica gel (250 μm) plates. UV light and/or iodine, potassium permanganate, and potassium iodoplatinate stains were used to visualize products. Medium pressure liquid chromatography was performed on a Biotage Isolera in conjunction with a Biotage Dalton 2000 using the conditions indicated. Nuclear magnetic resonance spectra (NMR) were acquired on a Bruker Avance-III-500 MHz spectrometer equipped with a TCI cryoprobe. ^1H and ^{13}C chemical shifts were measured relative to residual solvent peaks as an internal standard set to δ 7.26 and δ 77.0 (CDCl$_3$), δ 2.50 and δ 39.5 (DMSO-d_6), or δ 3.31 and δ 49.00 (CD$_3$OD). Low-resolution mass spectra were recorded on a Biotage Dalton 2000 or Advion Expression Compact Mass Spectrometer using the indicated ionization method. High-resolution mass spectra were recorded at the Indiana University Mass Spectrometry Facility on a Thermo Scientific Orbitrap XL spectrometer using the indicated ionization method. Post-acquisition gain correction was applied using reserpine as a lock mass.

### General procedure-a for the preparation of compounds 2a-d

N-(10-bromodecyl)phthalimide (1 equiv, Combi-Blocks, Inc., cat # QI-5596) was dissolved in anhydrous acetonitrile (CH$_3$CN) (Sigma-Aldrich, cat # 271004-1L) or N,N-dimethylformide (DMF) (Sigma-Aldrich, cat# 227056-1L) (0.32 M) and placed under nitrogen. This was treated with the indicated phosphine (1 equiv). The reaction was then heated at reflux for CH$_3$CN or in a pressure vessel at 140°C for DMF for 18-51 h. The reaction was then concentrated in vacuo to give crude 2a-d. The material was purified by silica

column chromatography (0-30% v/v MeOH (Sigma- Aldrich, cat # 179337)/dichloromethane (DCM) (Sigma-Aldrich, cat #D65100)) to provide the title compound.
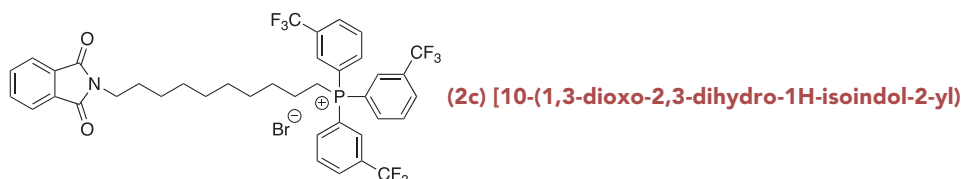

(2a) [10-(1,3-dioxo-2,3-dihydro-1H-isoindol-2-yl)decyl]
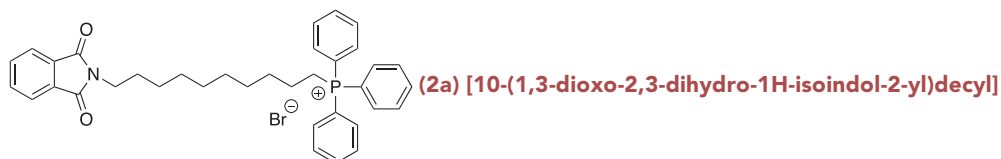
triphenylphosphonium bromide

A mixture of 2.5 g (6.83 mmol) of N-(10-bromodecyl)phthalimide in CH$_3$CN (21 mL) was refluxed with triphenylphosphine (Oakwood, cat # 037818) for 18 h. Flash chromatography gave 3.98 g (93%) of the title compound. Spectra match those previously reported.[21]


(2b) [10-(1,3-dioxo-2,3-dihydro-1H-isoindol-2-yl)
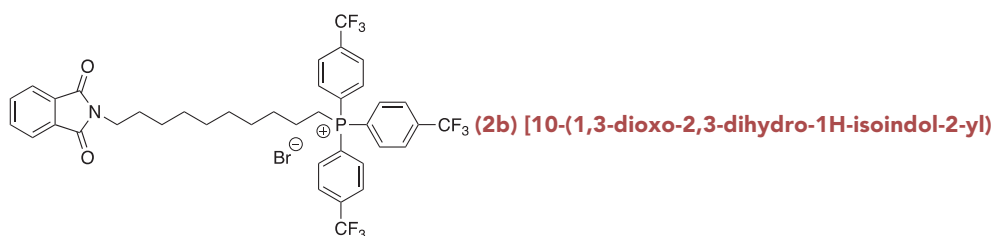
decyl]tris[4-(trifluoromethyl)phenyl]-phosphonium bromide

A mixture of 1.5 g (4.10 mmol) of N-(10-bromodecyl)phthalimide in DMF (12.6 mL) was heated with tris(4-trifluoromethyl)phosphine (1.91 g, 4.10 mmol, Ambeed, cat # A108436) for 51 h. Flash chromatography gave 2.59 g (76%) of the title compound. Spectra match those previously reported.[21]

(2c) [10-(1,3-dioxo-2,3-dihydro-1H-isoindol-2-yl)

decyl]tris[3-(trifluoromethyl)phenyl]-phosphonium bromide

A mixture of 0.500 g (1.37 mmol) of N-(10-bromodecyl)phthalimide in DMF (12.6 mL) was heated with tris(3-trifluoromethyl)phosphine[45] (0.637 g, 1.37 mmol) for 51 h. Flash chromatography gave 0.442 g (76%) of the title compound.


(2d) [10-(1,3-dioxo-2,3-dihydro-1H-isoindol-2-
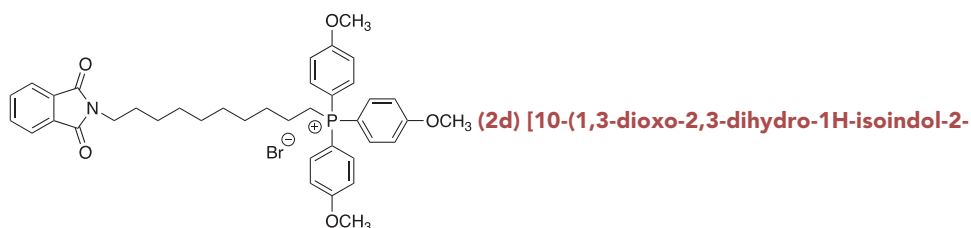
yl)decyl]tris(4-methoxyphenyl)phosphonium bromide

A mixture of 0.500 g (1.37 mmol) of N-(10-bromodecyl)phthalimide in CH$_3$CN (4.2 mL) was refluxed with tris(4-methoxyphenyl)phosphine (Ambeed, cat # A354955) for 19 h. Flash chromatography gave 0.920 g (93%) of the title compound. ^{1}H NMR (500 MHz, DMSO) δ 7.92–7.85 (m, 4H), 7.69 (dd, J = 10.3, 10.3 Hz, 6H), 7.32 (dd, J = 2.1, 8.8 Hz, 6H), 3.92 (s, 9H), 3.58 (t, J = 7.1 Hz, 2H), 1.59 (m, J = 7.1 Hz, 2H), 1.54–1.40 (m, 5H), 1.32–1.17 (m, 11H).

### General Procedure-B for the preparation of compounds 4a-c

Compound 2a-c (1 equiv) was dissolved in EtOH (0.16 M, Decon Labs, inc. cat # UN1987) and placed under nitrogen. This was treated with hydrazine (1 equiv or 1.5 equiv, Sigma-Aldrich, cat # 21555). The reaction

was then heated to reflux for 20 h. The reaction was then concentrated, and the byproduct was precipitated using EtOH/Et$_2$O Sigma-Aldrich, cat # 673811) and removed by vacuum filtration to give crude intermediate 3a-d. The material was purified by silica column chromatography using amine-treated silica (0-20% v/v MeOH/DCM). The residue (1 equiv) was dissolved in *n*-BuOH (0.24 M, Sigma-Aldrich, cat # 360465) and placed under nitrogen. This was treated with *N*-[amino(methylsulfanyl)methylidene]guanidine hydroiodide[46] (1.15 equiv). The reaction was heated to 130°C for 3 h and concentrated. The material was purified by silica column chromatography using amine-treated silica (1-20% v/v MeOH/DCM) to give the title compound.

(4a, MMe) 10-[(carbamimidamidomethanimidoyl)
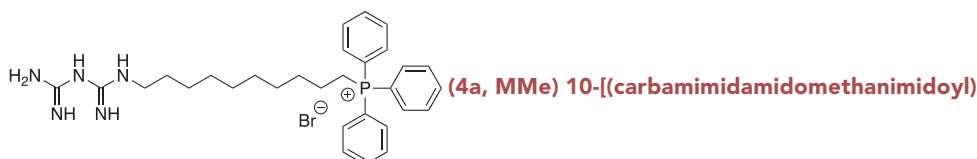
amino]decyl-triphenylphosphonium bromide

A mixture of 2a (1.5 g, 2.39 mmol) and hydrazine (0.074 mL, 2.39 mmol) was refluxed in ethanol (15 mL) for 20 h. Purification by silica column chromatography afforded the amine as an amorphous solid, which was carried forward without further manipulation. LRMS (+ESI) *m/z* [M−Br]$^+$, Calculated for C$_{28}$H$_{37}$NP 418.3; Found 418.4. A mixture of 0.906 g (1.82 mmol) of (10-aminodecyl)triphenylphosphonium in *n*-BuOH (7.5 mL) was heated with *N*-[amino(methylsulfanyl)methylidene]guanidine hydroiodide (0.543 g, 2.09 mmol). Flash chromatography gave 0.367 g (35%) of the title compound as an amorphous solid. HRMS (+ESI) *m/z*: [M−Br]$^+$ calculated for C$_{30}$H$_{41}$N$_5$P 502.3094; Found 502.3094.

(4b, *p*CF$_3$-MMe) (10-(3-carbamimidoylguanidino)
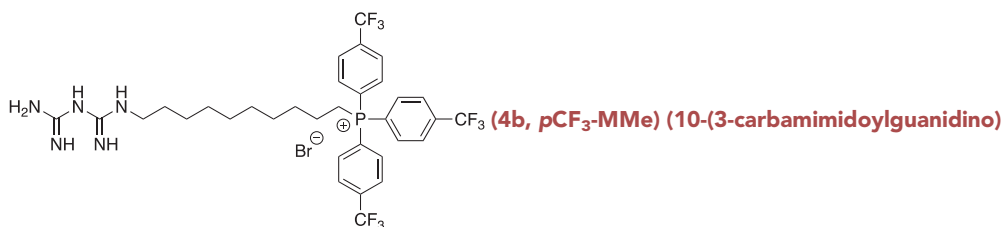
### decyl)tris(4-(trifluoromethyl)phenyl)phosphonium bromide

A mixture of 2b (2.59 g, 3.11 mmol) and hydrazine (0.145 mL, 4.66 mmol) was refluxed in ethanol (19 mL) for 20 h. Purification by silica column chromatography afforded the amine as an amorphous solid, which was carried forward without further manipulation. LRMS (+ESI) *m/z* [M−Br]$^+$, Calculated for C$_{31}$H$_{34}$F$_9$NP 622.2; Found 622.2. A mixture of 0.630 g (0.879 mmol) of (10-aminodecyl)tris[4-(trifluoromethyl)phenyl]phosphonium bromide in *n*-BuOH (3.7 mL) was heated with *N*-[amino(methylsulfanyl)methylidene]guanidine hydroiodide (0.268 g, 1.03 mmol). Flash chromatography gave 0.224 g (32%) of the title compound as an amorphous solid. ^{1}H NMR (500 MHz, CD$_3$OD) δ 8.06–7.73 (12H, m), 3.26–3.19 (2H, m), 3.12–3.05 (1H, m), 2.97–2.90 (4H, m), 2.51–2.40 (1H, m),1.55–1.29 (6H, m), 1.29–1.10 (10H, m). ^{19}F NMR (470 MHz, CD$_3$OD) δ −64.66. HRMS (+ESI) *m/z*: [M−Br]$^+$ calculated for C$_{33}$H$_{38}$F$_9$N$_5$P 706.2716; Found 706.2722.

(4c, *m*CF$_3$-MMe) (10-(3-carbamimidoylguanidino)

decyl)tris(3-(trifluoromethyl)phenyl)phosphonium bromide

A mixture of 2c (0.4421 g, 0.531 mmol) and hydrazine (0.025 mL, 0.796 mmol) was refluxed in ethanol for 20 h. Purification by silica column chromatography afforded the amine as an amorphous solid, which was carried forward without further manipulation. LRMS (+ESI) *m/z* [M−Br]$^+$, Calculated for C$_{31}$H$_{34}$F$_9$NP 622.2; Found 622.2. A mixture of 0.069 g (0.098 mmol) of (10-aminodecyl)tris[3-(trifluoromethyl)phenyl]phosphonium bromide in *n*-BuOH (1 mL) was heated with *N*-[amino(methylsulfanyl)methylidene]guanidine hydroiodide (0.029 g, 0.113 mmol). Flash chromatography gave 0.006 g (7%) of the title compound as an amorphous solid. ^{1}H NMR (500 MHz, DMSO-*d$_6$*) δ 8.40–7.62 (6H, m), 6.71–6.53 (10H, m), 1.64–1.14

(16H, m). ^{19}F NMR (470 MHz, CD$_3$OD) δ −61.19. Significant ^{31}P splitting complicated the proton spectrum. HRMS (+ESI) m/z: [M−Br]$^+$ Calculated for C$_{33}$H$_{38}$F$_9$N$_5$P 706.2716; Found 706.2713.

(4d, pMeO-MMe) [10-(2-carbamimidoyle
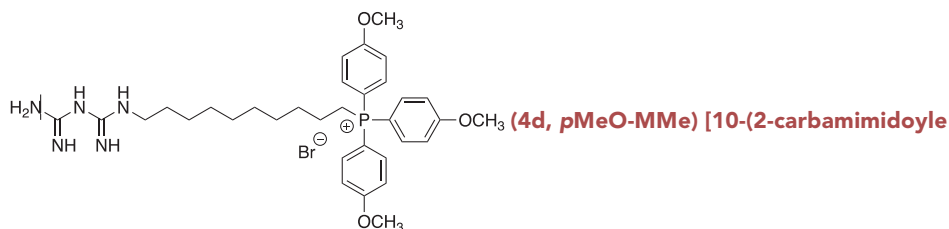
thanimidamido)decyl]tris(4-methoxyphenyl)phosphonium bromide

Compound 2days (0.920 g, 1.28 mmol) was dissolved in EtOH (8 mL) and placed under nitrogen. This was treated with hydrazine (0.040 mL, 1.28 mmol). The reaction was then heated to reflux for 20 h. The reaction was then concentrated, and the byproduct was precipitated using EtOH/Et$_2$O and removed by vacuum filtration. The filtrate was concentrated *in vacuo* to give crude intermediate 3days. Intermediate 3d (0.150 g, 0.255 mmol) was dissolved in CH$_2$Cl$_2$ (2.5 mL) and cooled to 0°C in an ice bath. This was treated with hydrogen chloride (0.765 mL, 0.765 mmol, 1 M in Et$_2$O, Sigma-Aldrich, cat # 294837) by dropwise addition. Once the addition was complete, the reaction was stirred at room temperature for 1 h. The reaction was then concentrated *in vacuo*. The resulting yellowish foam was dissolved in anhydrous DMF (1.0 mL) and treated with cyanoguanidine (0.096 g, 1.47 mmol, Sigma-Aldrich, cat #D76609). The reaction was then heated to 160°C for 2 h. The reaction was concentrated *in vacuo*. The material was purified by silica column chromatography using amine-treated silica (1-30% v/v MeOH/DCM) to give 0.114 g (67%) of the title compound. ^{1}H NMR (500 MHz, CD$_3$OD) δ 7.61–7.47 (6H, m), 7.21–7.08 (6H, m), 3.83 (9H, s), 3.26–3.19 (2H, m), 3.12–3.05 (3H, m), 3.02–2.91 (6H, m), 1.60–1.50 (2H, m),1.47–1.35 (4H, m), 1.30–1.11 (10H, m). HRMS (+ESI) m/z: [M−Br]$^+$ calculated for C$_{33}$H$_{47}$N$_3$O$_5$ 592.3411; Found 592.3409.

Statistical analyses

All statistical analyses were performed using GraphPad Prism (La Jolla, CA). Unpaired analyses were calculated using Student's *t* test to identify pairwise differences between experimental and control groups. Values provided represent mean ± SD. Statistical significance was defined as p ≤ 0.05 and denoted with asterisks as indicated in the figure legends.